Mobility Enhancement in Graphene by *in situ* Reduction of Random Strain Fluctuations

Lujun Wang (王律俊),[1,2,*] Péter Makk,[1,3,†] Simon Zihlmann,[1] Andreas Baumgartner,[1,2] David I. Indolese,[1] Kenji Watanabe,[4] Takashi Taniguchi,[4] and Christian Schönenberger[1,2]

[1]*Department of Physics, University of Basel, Klingelbergstrasse 82, CH-4056 Basel, Switzerland*
[2]*Swiss Nanoscience Institute, University of Basel, Klingelbergstrasse 82, CH-4056 Basel, Switzerland*
[3]*Department of Physics, Budapest University of Technology and Economics and Nanoelectronics Momentum Research Group of the Hungarian Academy of Sciences, Budafoki ut 8, 1111 Budapest, Hungary*
[4]*National Institute for Material Science, 1-1 Namiki, Tsukuba, 305-0044, Japan*

(Received 30 September 2019; accepted 16 March 2020; published 15 April 2020)

Microscopic corrugations are ubiquitous in graphene even when placed on atomically flat substrates. These result in random local strain fluctuations limiting the carrier mobility of high quality hBN-supported graphene devices. We present transport measurements in hBN-encapsulated devices where such strain fluctuations can be *in situ* reduced by increasing the average uniaxial strain. When ~0.2% of uniaxial strain is applied to the graphene, an enhancement of the carrier mobility by ~35% is observed while the residual doping reduces by ~39%. We demonstrate a strong correlation between the mobility and the residual doping, from which we conclude that random local strain fluctuations are the dominant source of disorder limiting the mobility in these devices. Our findings are also supported by Raman spectroscopy measurements.

DOI: 10.1103/PhysRevLett.124.157701

In the first generation of graphene devices, where SiO_2 was used as the substrate, it is commonly believed that random charged impurities at the substrate surface are the dominant source of disorder limiting the device quality [1–7]. One way to improve the device quality is to suspend graphene to spatially separate it from the charge traps [8–12]. Nowadays, a more widely used technique is to place graphene on hexagonal boron nitride (hBN) [13–16], which is atomically flat and expected to be free of surface charge traps. A significant improvement in device quality has been achieved, exhibiting very high carrier mobilities, enabling the observation of a series of new physical phenomena, such as the fractional quantum Hall effect [17–19], transverse magnetic focusing [20–22] and various moiré superlattice effects [23–26]. Although the mobility of hBN-supported graphene devices is generally higher than that of the SiO_2-supported, the reported mobility values vary over a large range, suggesting another mechanism that limits the mobility. It has been pointed out that random strain fluctuations (RSFs) in graphene could be a dominant source of disorder leading to electron scattering [27–29]. In a recent statistical study of many devices on hBN substrates, a clear correlation between the carrier mobility μ and the residual doping n_0 was found, pointing to RSFs as the dominant microscopic source of scattering [30]. The residual doping caused by charge fluctuations manifests in a broadening of the resistance peak around the charge neutrality point (CNP). Similar results have been found as well in bilayer graphene [31].

Ripples and pronounced corrugations can form naturally in graphene due to its two-dimensional nature, as, for example, demonstrated by transmission electron microscopy in suspended graphene membranes [32]. In stacked layers, microscopic corrugations can spontaneously form during exfoliation due to thermal fluctuations at room temperature [27,33,34]. These corrugations might persist through the fabrication processes and give rise to RSFs in the final device. In SiO_2-supported devices, nanometer-scale ripples have been observed in scanning probe microscopy studies [35–38] and their effects on electron transport have been reported in weak localization studies [39–41]. Although the hBN surface is typically much flatter, height fluctuations are still present in hBN-supported graphene devices [13], which can result in RSFs. These RSFs have been confirmed in Raman spectroscopy measurements [42,43].

Here we demonstrate in a direct experiment that RSFs can be the mechanism limiting the mobility of encapsulated devices. We compare the transport characteristics of individual devices before and after increasing the average uniaxial strain, which directly reduces the strain fluctuations in the same device. In Fig. 1(c) the RSFs in graphene lattice are illustrated, which we believe can be reduced gradually by increasing the average strain, as indicated by the arrows. The reduction of the RSFs due to increasing average strain is further confirmed by directly probing the RSFs using Raman spectroscopy [42]. This not only allows us to determine the dominant microscopic mechanism, but also to actually increase the mobility of the device.

The setup of the experiment is shown schematically in Figs. 1(a), 1(b). It allows us to tune the average uniaxial strain in hBN-encapsulated graphene devices by bending a flexible substrate [44]. The displacement Δz of the pushing wedge relative to the mounting position determines the

 © 2020 American Physical Society

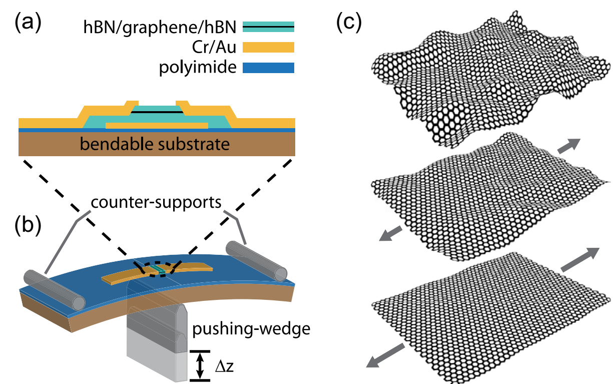

FIG. 1. Schematics of (a) the device cross section and (b) the three-point bending setup. The bending of the substrate is determined by the displacement of the pushing wedge Δz. (c) Illustration of the effects of reducing the strain fluctuations. The arrows indicate the direction and the strength of the externally induced strain by substrate bending mediated by contacts.

deformation of the substrate and is used to tune the average strain in the graphene. The devices are fabricated using a dry-transfer method [16], where we pick up a ~20 nm thick hBN as the top layer, then an exfoliated monolayer graphene flake from natural graphite and a ~30 nm thick hBN as the bottom layer. The assembled stack is then deposited onto a metallic gate structure prefabricated on a polyimide-coated phosphor bronze plate. Edge contacts [16] (Cr/Au, 5 nm/110 nm) are made with a controlled etching recipe, which stops in the middle of the bottom hBN, with the remaining hBN acting as the insulating layer between the contacts and the bottom gate [44]; see Fig. 1(a).

To investigate the effects of average strain on the transport characteristics of graphene, we measure the two-terminal differential conductance G as a function of the gate voltage V_g for different Δz values, as plotted in Fig. 2(a). The measurements were performed at low temperature ($T = 4.2$ K) using standard low-frequency lock-in techniques. The CNP is at $V_g = 0.4$ V, indicating an offset p doping in our device. The conductance of the graphene increases faster when gated away from the CNP for larger Δz, suggesting an increase in field effect mobility with increasing Δz. This effect is reversible when Δz is decreased and is reproducible after many straining cycles (see Supplemental Material [45]). A displacement of $\Delta z = 0.6$ mm corresponds to ~0.2% of average strain, which is determined from Raman measurements shown later [44]. The conductance starts to saturate at higher gate voltages because of the contact resistance. On the hole side (p doping), a p-n junction forms near each contact due to the n doping from the contact, resulting in a sightly larger contact resistance and a lower saturation conductance, which renders the mobility change less visible. The zoomed-in data in the inset of Fig. 2(a) shows qualitatively the same effect as for the electron side.

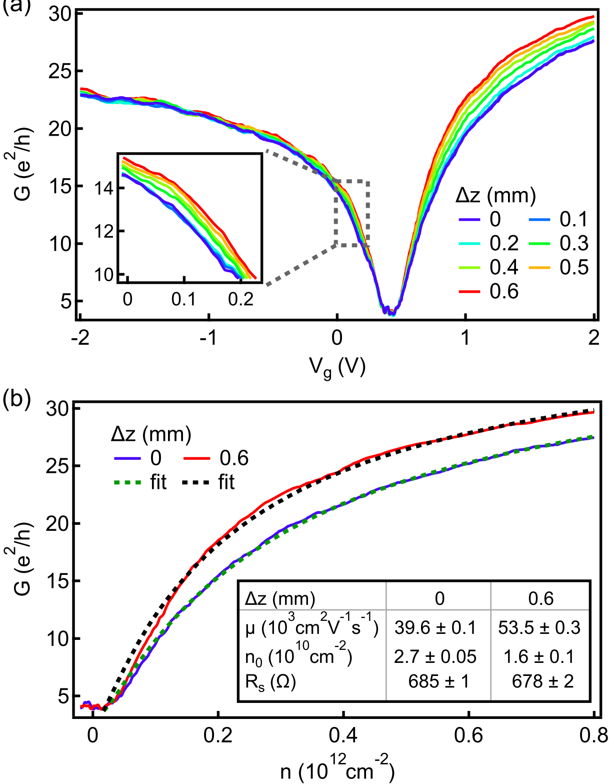

FIG. 2. (a) Two-terminal differential conductance G plotted as a function of gate voltage V_g for different Δz values. The slope of the curves becomes steeper for larger Δz, for both the electron and hole side. The inset shows an enlargement to the hole side. (b) G versus n for two different Δz on the electron side. The fits according to Eq. (1) are shown as dashed lines for $\Delta z = 0$ and 0.6 mm, respectively, with the fitting parameters given in the table.

To quantitatively evaluate the effects of strain tuning on the electrical properties of graphene, we fit each curve on the electron side (n doping) with the following formula based on the Drude model [7,13]:

$$G = \frac{1}{\frac{\alpha}{e\mu\sqrt{n^2+n_0^2}} + R_s}, \tag{1}$$

where e is the elementary charge and α is the geometry factor describing the aspect ratio, which is 1.28 in this case (see Supplemental Material [45]). The fitting parameters are the charge-carrier density independent mobility μ, the residual doping n_0 around the CNP, and the serial resistance R_s (discussion on the serial resistance is given in the Supplemental Material [45]). The charge-carrier density n is calculated from the applied gate voltage V_g with a lever arm of 5.13×10^{11} cm^{-2} V^{-1} using a parallel plate capacitor model. The thickness of the bottom hBN, which is the gate dielectric, is determined by atomic force microscopy. Two examples of the fitting are shown as dashed lines for

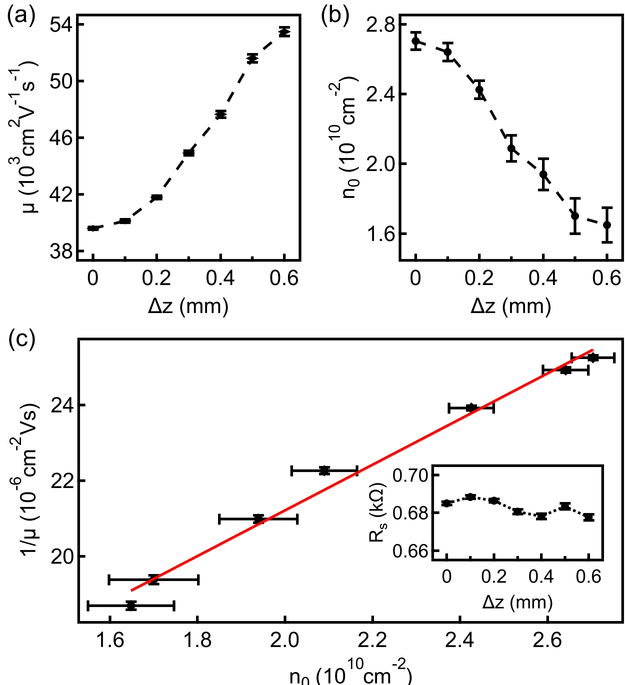

FIG. 3. (a) Extracted field effect mobility μ and (b) residual doping n_0 values from fitting plotted as a function of Δz on the electron side. The error bars are the standard errors from fits. The mobility μ shows an increase with increasing Δz while n_0 shows a decrease. (c) Data of (a) and (b) plotted as $1/\mu$ versus n_0, showing a clear linear relation. The red line is a linear fit to the data with $1/\mu = (0.146 \pm 0.007) \times (h/e)n_0 + 1/\mu_0$ and $\mu_0 \approx 110\,000$ cm^2 V^{-1} s^{-1}. The inset shows the extracted serial resistance R_s (including contact resistance and ~350 Ω line resistance) for different Δz.

$\Delta z = 0$ and 0.6 mm in Fig. 2(b) with the corresponding parameters given in the inset.

The fitting results for μ and n_0 are plotted as a function of Δz in Figs. 3(a), 3(b), respectively. The mobility μ shows a clear increase with increasing Δz, while n_0 decreases significantly. The change is slower in the beginning, which might be attributed to a small mechanical hysteresis of the bending setup. The extracted serial resistance R_s (including contact resistance and ~350 Ω line resistance) is shown in the inset of Fig. 3(c) and is essentially unaffected by the bending, demonstrating the mechanical robustness of the device for these levels of applied average strain [44]. The mobility increases from ~40 000 to ~54 000 cm^2 V^{-1} s^{-1} when Δz is increased from 0 to 0.6 mm. At the same time the residual doping drops gradually from $\sim 2.7 \times 10^{10}$ cm^{-2} at $\Delta z = 0$ to $\sim 1.6 \times 10^{10}$ cm^{-2} at $\Delta z = 0.6$ mm (another independent procedure for extracting the residual doping is shown in the Supplemental Material [45]). The (μ, n_0) pairs are plotted as $1/\mu$ versus n_0 in Fig. 3(c), clearly demonstrating the proportionality between $1/\mu$ and n_0. The same analysis is performed for the hole side and similar results are obtained with a larger serial resistance (see Supplemental Material [45]), which is consistent with the interpretation that the p-n junction makes the effect less pronounced on the hole side.

Since the graphene is encapsulated with hBN, the possible strain-induced redistribution of impurities, such as contaminants or resist residuals from fabrication processes, should not affect the charge transport in graphene. It is also very unlikely that the small applied average strain changes the charged impurities at the graphene-hBN interfaces, ruling them out as the dominant mechanism for the observed mobility increase. On the other hand, even if the redistribution of impurities would be relevant, it should lead to a random change of the conductance with strain instead of a monotonic and systematic effect observed here. An artificial effect due to the change of the gate capacitance with strain is also ruled out [44], because the CNP appears at the same gate voltage for all Δz values.

RSFs have been identified theoretically as a possible source of disorder limiting charge carrier mobility [27,28]. Strong evidence of this mechanism has been found in a statistical study involving many devices, where a clear linear relation between $1/\mu$ and n_0 was observed, with $1/\mu \approx 0.118 \times (h/e)n_0$ [30]. Moreover, a detailed microscopic mechanism was proposed in which the variation of n_0 was attributed to RSFs-induced scalar potentials, while the limitation in μ was attributed to randomly varying pseudomagnetic fields [30]. Fitting our data linearly in Fig. 3(c) yields $1/\mu = (0.146 \pm 0.007) \times (h/e)n_0 + 1/\mu_0$ and $\mu_0 \approx 110\,000$ cm^2 V^{-1} s^{-1}. It shows a similar slope [$\sim 0.146 \times (h/e)$], allowing us to draw two conclusions. First, the charge carrier mobility is limited by RSFs and second, the control of the average strain allows us to control the RSFs and hence the mobility. The offset $1/\mu_0$ might imply another mobility limiting mechanism when RSFs are not dominating anymore. The value $\mu_0 \approx 110\,000$ cm^2 V^{-1} s^{-1} nearly coincides with the mobility of the devices, in which no mobility enhancement due to increasing average strain is observed (discussed later).

Theoretically both in-plane and out-of-plane strain fluctuations can contribute to this effect [30]. In a previous study of weak localization on SiO_2-supported graphene devices [41], a reduction of the phase coherence time τ_ϕ was found for an increasing in-plane magnetic field. It has been attributed to an enhanced dephasing rate due to a random vector potential generated by the in-plane magnetic field penetrating out-of-plane corrugations in the graphene layer. Similar effects have been observed in encapsulated devices [50,51], strongly suggesting that out-of-plane corrugations are also present in encapsulated graphene. We therefore attribute the mobility increase in our experiment to the reducing of out-of-plane strain fluctuations, as illustrated in Fig. 1(c).

To further substantiate our findings, we use spatially resolved Raman spectroscopy to directly probe the RSFs at room temperature. For small uniaxial strain, which is the case in our experiment, the graphene Raman 2D peak can

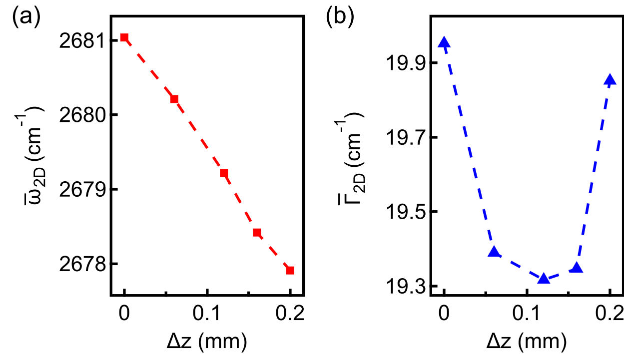

FIG. 4. (a) Spatially averaged center frequency $\bar{\omega}_{2D}$ of the Raman 2D peak for different Δz, showing a linear decrease with increasing Δz, which suggests an increasing average strain. (b) Spatially averaged linewidth $\bar{\Gamma}_{2D}$ of the Raman 2D peak as a function of Δz, exhibiting nonmonotonic characteristics with a minimum of $\sim 19.3\ \mathrm{cm}^{-1}$.

be fitted by a single Lorentzian [52], with a center frequency ω_{2D} and linewidth Γ_{2D}. The center frequency ω_{2D} redshifts with increasing strain, while the linewidth Γ_{2D} broadens due to the splitting of the 2D peak [53,54]. It has been shown that nanometer-scale strain inhomogeneities within the laser spot ($\sim$500 nm) also broadens the 2D peak [42], originating from averaging over regions with different local strain and hence different ω_{2D}. Therefore, Γ_{2D} can be used to probe the RSFs. We perform spatially resolved Raman spectroscopy and extract maps of ω_{2D} and Γ_{2D} for different Δz. The mean value of the center frequency $\bar{\omega}_{2D}$ averaged over the whole device is plotted as a function of Δz in Fig. 4(a). It shifts linearly to lower values with increasing Δz, indicating an increasing average strain in the graphene sheet [52]. The $\sim 3\ \mathrm{cm}^{-1}$ shift at $\Delta z = 0.2$ mm corresponds to an externally induced average strain of $\sim$0.06% [44]. In Fig. 4(b) the averaged value of the 2D peak linewidth $\bar{\Gamma}_{2D}$ is plotted as a function of Δz, showing nonmonotonic characteristics with a minimum of $\sim 19.3\ \mathrm{cm}^{-1}$ at $\Delta z = 0.12$ mm. It first decreases with increasing Δz before increasing again, which can be explained by the competition between the two broadening mechanisms. The initial value of $\bar{\Gamma}_{2D}$ ($\sim 20\ \mathrm{cm}^{-1}$) is larger than the intrinsic linewidth ($\sim 17\ \mathrm{cm}^{-1}$) of the 2D peak [42], indicating that RSFs are present in our graphene. We attribute the decrease of $\bar{\Gamma}_{2D}$ to a reduction of the RSFs due to the externally applied strain, as illustrated in Fig. 1(c). When the broadening of the 2D peak induced by the increasing average strain dominates, $\bar{\Gamma}_{2D}$ increases again with increasing Δz.

Our interpretation is also consistent with weak localization measurements we performed to extract characteristic scattering times (see Supplemental Material [45]). We find that the intervalley scattering time τ_{iv} is much longer than the elastic scattering time τ (determined from the mobility), implying that the mobility is not limited by intervalley scattering processes (scattering on short-range potentials, e.g., defects, edges). In contrast, the intravalley scattering time τ_* (the time needed to break the effective single-valley time-reversal symmetry) is nearly identical to τ, pointing to RSFs-induced random pseudomagnetic fields as the main factors limiting the mobility [30]. For charged impurities, it has been argued that $\tau_* \gg \tau$ [30], which is not the case here.

We have observed a clear increase in the mobility with increasing average strain in more than 5 devices with their mobility values varying from $\sim$30 000 to $\sim 80\,000\ \mathrm{cm}^2\,\mathrm{V}^{-1}\,\mathrm{s}^{-1}$. In Fig. 3(a), there is also an indication that the mobility starts to saturate when it approaches higher values. For the devices with a mobility larger than $\sim 80\,000\ \mathrm{cm}^2\,\mathrm{V}^{-1}\,\mathrm{s}^{-1}$, the mobility-increase effect is absent. (Examples are presented in the Supplemental Material [45].) These observations suggest that either some residual RSFs cannot be fully removed by increasing the average strain, or more probably, that other scattering mechanisms than RSFs limit the mobility in ultra high mobility devices, e.g., scattering at the geometrical boundaries of the devices.

In conclusion, we have demonstrated an *in situ* reduction of the RSFs in individual encapsulated graphene devices by increasing the average strain. In low-temperature transport measurements, an enhancement of the carrier mobility by $\sim$35% is observed while the residual doping reduces by $\sim$39% when $\sim$0.2% of average strain is applied to the graphene. The linear correlation between $1/\mu$ and n_0 and the fact that τ is limited by τ_* reveal that RSFs are the dominant scattering mechanism. These findings are further substantiated by Raman spectroscopy, in which the 2D peak linewidth Γ_{2D}, first decreases with increasing average strain before the average strain induced broadening dominates. The *in situ* straining allows us to directly compare results on individual devices and to avoid statistics over different devices. Using this technique we have directly confirmed that RSFs are the dominant scattering mechanism limiting the mobility in most hBN-supported graphene devices. For devices with even higher mobilities, either the reduction of RSFs is not possible, or another scattering mechanism becomes dominant.

All data in this publication are available in numerical form at Ref. [55].

This work has received funding from the Swiss Nanoscience Institute (SNI), the ERC project TopSupra (787414), the European Union Horizon 2020 research and innovation programme under Grant Agreement No. 785219 (Graphene Flagship), the Swiss National Science Foundation, the Swiss NCCR QSIT, Topograph, ISpinText FlagERA network and from the OTKA FK-123894 grants. P. M. acknowledges support from the Bolyai Fellowship, the Marie Curie grant and the National Research, Development and Innovation Fund of Hungary within the Quantum Technology National Excellence Program (Project No. 2017-1.2.1-NKP-2017-00001). K. W. and T. T. acknowledge support from the

Elemental Strategy Initiative conducted by the MEXT, Japan and the CREST (JPMJCR15F3), JST. The authors thank Francisco Guinea and Peter Rickhaus for fruitful discussions, and Sascha Martin and his team for their technical support. L. W. fabricated the devices, performed the measurements and did the data analysis. P. M. helped to understand the data. P. M., S. Z., and A. B. helped with the data analysis. P. M., S. Z., and D. I. supported the device fabrication. K. W. and T. T. provided high-quality hBN. C. S. initiated and supervised the project. L. W. wrote the paper and all authors discussed the results and worked on the manuscript.

*lujun.wang@unibas.ch
†peter.makk@unibas.ch

[1] T. Ando, J. Phys. Soc. Jpn. **75**, 074716 (2006).
[2] K. Nomura and A. H. MacDonald, Phys. Rev. Lett. **98**, 076602 (2007).
[3] E. H. Hwang, S. Adam, and S. D. Sarma, Phys. Rev. Lett. **98**, 186806 (2007).
[4] S. Adam, E. H. Hwang, V. M. Galitski, and S. D. Sarma, Proc. Natl. Acad. Sci. U.S.A. **104**, 18392 (2007).
[5] J.-H. Chen, C. Jang, S. Adam, M. S. Fuhrer, E. D. Williams, and M. Ishigami, Nat. Phys. **4**, 377 (2008).
[6] J.-H. Chen, C. Jang, S. Xiao, M. Ishigami, and M. S. Fuhrer, Nat. Nanotechnol. **3**, 206 (2008).
[7] X. Hong, K. Zou, and J. Zhu, Phys. Rev. B **80**, 241415(R) (2009).
[8] K. Bolotin, K. Sikes, Z. Jiang, M. Klima, G. Fudenberg, J. Hone, P. Kim, and H. Stormer, Solid State Commun. **146**, 351 (2008).
[9] X. Du, I. Skachko, A. Barker, and E. Y. Andrei, Nat. Nanotechnol. **3**, 491 (2008).
[10] K. I. Bolotin, K. J. Sikes, J. Hone, H. L. Stormer, and P. Kim, Phys. Rev. Lett. **101**, 096802 (2008).
[11] N. Tombros, A. Veligura, J. Junesch, J. J. van den Berg, P. J. Zomer, M. Wojtaszek, I. J. Vera Marun, H. T. Jonkman, and B. J. van Wees, J. Appl. Phys. **109**, 093702 (2011).
[12] R. Maurand, P. Rickhaus, P. Makk, S. Hess, E. Tvri, C. Handschin, M. Weiss, and C. Schnenberger, Carbon **79**, 486 (2014).
[13] C. R. Dean, A. F. Young, I. Meric, C. Lee, L. Wang, S. Sorgenfrei, K. Watanabe, T. Taniguchi, P. Kim, K. L. Shepard, and J. Hone, Nat. Nanotechnol. **5**, 722 (2010).
[14] P. J. Zomer, S. P. Dash, N. Tombros, and B. J. van Wees, Appl. Phys. Lett. **99**, 232104 (2011).
[15] A. S. Mayorov, R. V. Gorbachev, S. V. Morozov, L. Britnell, R. Jalil, L. A. Ponomarenko, P. Blake, K. S. Novoselov, K. Watanabe, T. Taniguchi, and A. K. Geim, Nano Lett. **11**, 2396 (2011).
[16] L. Wang, I. Meric, P. Y. Huang, Q. Gao, Y. Gao, H. Tran, T. Taniguchi, K. Watanabe, L. M. Campos, D. A. Muller, J. Guo, P. Kim, J. Hone, K. L. Shepard, and C. R. Dean, Science **342**, 614 (2013).
[17] K. I. Bolotin, F. Ghahari, M. D. Shulman, H. L. Stormer, and P. Kim, Nature (London) **462**, 196 (2009).
[18] X. Du, I. Skachko, F. Duerr, A. Luican, and E. Y. Andrei, Nature (London) **462**, 192 (2009).
[19] C. R. Dean, A. F. Young, P. Cadden-Zimansky, L. Wang, H. Ren, K. Watanabe, T. Taniguchi, P. Kim, J. Hone, and K. L. Shepard, Nat. Phys. **7**, 693 (2011).
[20] T. Taychatanapat, K. Watanabe, T. Taniguchi, and P. Jarillo-Herrero, Nat. Phys. **9**, 225 (2013).
[21] M. Lee, J. R. Wallbank, P. Gallagher, K. Watanabe, T. Taniguchi, V. I. Fal'ko, and D. Goldhaber-Gordon, Science **353**, 1526 (2016).
[22] S. Chen, Z. Han, M. M. Elahi, K. M. M. Habib, L. Wang, B. Wen, Y. Gao, T. Taniguchi, K. Watanabe, J. Hone, A. W. Ghosh, and C. R. Dean, Science **353**, 1522 (2016).
[23] L. A. Ponomarenko, R. V. Gorbachev, G. L. Yu, D. C. Elias, R. Jalil, A. A. Patel, A. Mishchenko, A. S. Mayorov, C. R. Woods, J. R. Wallbank, M. Mucha-Kruczynski, B. A. Piot, M. Potemski, I. V. Grigorieva, K. S. Novoselov, F. Guinea, V. I. Falko, and A. K. Geim, Nature (London) **497**, 594 (2013).
[24] C. R. Dean, L. Wang, P. Maher, C. Forsythe, F. Ghahari, Y. Gao, J. Katoch, M. Ishigami, P. Moon, M. Koshino, T. Taniguchi, K. Watanabe, K. L. Shepard, J. Hone, and P. Kim, Nature (London) **497**, 598 (2013).
[25] B. Hunt, J. D. Sanchez-Yamagishi, A. F. Young, M. Yankowitz, B. J. LeRoy, K. Watanabe, T. Taniguchi, P. Moon, M. Koshino, P. Jarillo-Herrero, and R. C. Ashoori, Science **340**, 1427 (2013).
[26] L. Wang, S. Zihlmann, M.-H. Liu, P. Makk, K. Watanabe, T. Taniguchi, A. Baumgartner, and C. Schönenberger, Nano Lett. **19**, 2371 (2019).
[27] M. Katsnelson and A. Geim, Phil. Trans. R. Soc. A **366**, 195 (2008).
[28] M. Gibertini, A. Tomadin, F. Guinea, M. I. Katsnelson, and M. Polini, Phys. Rev. B **85**, 201405(R) (2012).
[29] Y. Kim, P. Herlinger, T. Taniguchi, K. Watanabe, and J. H. Smet, ACS Nano **13**, 14182 (2019).
[30] N. J. G. Couto, D. Costanzo, S. Engels, D.-K. Ki, K. Watanabe, T. Taniguchi, C. Stampfer, F. Guinea, and A. F. Morpurgo, Phys. Rev. X **4**, 041019 (2014).
[31] S. Engels, B. Terrés, A. Epping, T. Khodkov, K. Watanabe, T. Taniguchi, B. Beschoten, and C. Stampfer, Phys. Rev. Lett. **113**, 126801 (2014).
[32] J. C. Meyer, A. K. Geim, M. I. Katsnelson, K. S. Novoselov, T. J. Booth, and S. Roth, Nature (London) **446**, 60 (2007).
[33] N. Abedpour, M. Neek-Amal, R. Asgari, F. Shahbazi, N. Nafari, and M. R. R. Tabar, Phys. Rev. B **76**, 195407 (2007).
[34] A. Fasolino, J. H. Los, and M. I. Katsnelson, Nat. Mater. **6**, 858 (2007).
[35] M. Ishigami, J. H. Chen, W. G. Cullen, M. S. Fuhrer, and E. D. Williams, Nano Lett. **7**, 1643 (2007).
[36] E. Stolyarova, K. T. Rim, S. Ryu, J. Maultzsch, P. Kim, L. E. Brus, T. F. Heinz, M. S. Hybertsen, and G. W. Flynn, Proc. Natl. Acad. Sci. U.S.A. **104**, 9209 (2007).
[37] V. Geringer, M. Liebmann, T. Echtermeyer, S. Runte, M. Schmidt, R. Rückamp, M. C. Lemme, and M. Morgenstern, Phys. Rev. Lett. **102**, 076102 (2009).
[38] W. G. Cullen, M. Yamamoto, K. M. Burson, J. H. Chen, C. Jang, L. Li, M. S. Fuhrer, and E. D. Williams, Phys. Rev. Lett. **105**, 215504 (2010).
[39] S. V. Morozov, K. S. Novoselov, M. I. Katsnelson, F. Schedin, L. A. Ponomarenko, D. Jiang, and A. K. Geim, Phys. Rev. Lett. **97**, 016801 (2006).

[40] F. V. Tikhonenko, D. W. Horsell, R. V. Gorbachev, and A. K. Savchenko, Phys. Rev. Lett. **100**, 056802 (2008).
[41] M. B. Lundeberg and J. A. Folk, Phys. Rev. Lett. **105**, 146804 (2010).
[42] C. Neumann, S. Reichardt, P. Venezuela, M. Drgeler, L. Banszerus, M. Schmitz, K. Watanabe, T. Taniguchi, F. Mauri, B. Beschoten, S. V. Rotkin, and C. Stampfer, Nat. Commun. **6**, 8429 (2015).
[43] L. Banszerus, H. Janssen, M. Otto, A. Epping, T. Taniguchi, K. Watanabe, B. Beschoten, D. Neumaier, and C. Stampfer, 2D Mater. **4**, 025030 (2017).
[44] L. Wang, S. Zihlmann, A. Baumgartner, J. Overbeck, K. Watanabe, T. Taniguchi, P. Makk, and C. Schnenberger, Nano Lett. **19**, 4097 (2019).
[45] See Supplemental Material at http://link.aps.org/supplemental/10.1103/PhysRevLett.124.157701 for additional information, which includes Refs. [46–49].
[46] S. V. Morozov, K. S. Novoselov, M. I. Katsnelson, F. Schedin, D. C. Elias, J. A. Jaszczak, and A. K. Geim, Phys. Rev. Lett. **100**, 016602 (2008).
[47] S. Fratini and F. Guinea, Phys. Rev. B **77**, 195415 (2008).
[48] E. McCann, K. Kechedzhi, V. I. Fal'ko, H. Suzuura, T. Ando, and B. L. Altshuler, Phys. Rev. Lett. **97**, 146805 (2006).
[49] A. Eckmann, J. Park, H. Yang, D. Elias, A. S. Mayorov, G. Yu, R. Jalil, K. S. Novoselov, R. V. Gorbachev, M. Lazzeri, A. K. Geim, and C. Casiraghi, Nano Lett. **13**, 5242 (2013).
[50] S. Zihlmann, A. W. Cummings, J. H. Garcia, M. Kedves, K. Watanabe, T. Taniguchi, C. Schönenberger, and P. Makk, Phys. Rev. B **97**, 075434 (2018).
[51] S. Zihlmann, P. Makk, M. K. Rehmann, L. Wang, M. Kedves, D. I. Indolese, K. Watanabe, T. Taniguchi, D. M. Zumbühl, and C. Schönenberger, arXiv:2004.02690.
[52] T. M. G. Mohiuddin, A. Lombardo, R. R. Nair, A. Bonetti, G. Savini, R. Jalil, N. Bonini, D. M. Basko, C. Galiotis, N. Marzari, K. S. Novoselov, A. K. Geim, and A. C. Ferrari, Phys. Rev. B **79**, 205433 (2009).
[53] M. Mohr, K. Papagelis, J. Maultzsch, and C. Thomsen, Phys. Rev. B **80**, 205410 (2009).
[54] M. Huang, H. Yan, T. F. Heinz, and J. Hone, Nano Lett. **10**, 4074 (2010).
[55] https://doi.org/10.5281/zenodo.3561000.